



Sediment plumes induced by the Port of Miami dredging: Analysis and interpretation using Landsat and MODIS data



Brian B. Barnes^{a,*}, Chuanmin Hu^a, Charles Kovach^a, Rachel N. Silverstein^b

^a College of Marine Science, University of South Florida, St Petersburg, FL USA

^b Miami Waterkeeper, Miami, FL USA

ARTICLE INFO

Article history:

Received 5 June 2015

Received in revised form 9 September 2015

Accepted 25 September 2015

Available online 9 October 2015

Keywords:

Turbidity,

Coral,

MODIS,

Landsat,

Dredging

ABSTRACT

Beginning in November 2013, large turbidity plumes were observed offshore the Port of Miami (Florida, USA), likely associated with a project to deepen and widen the Miami Harbor channels. Local coral colonies, including those considered threatened by the US Endangered Species Act, exacerbate the need for thorough assessment of these plumes. Without ruling out other causal factors such as wind storms and tidal currents, it is difficult to conclude whether the plumes were caused by the dredging. From current in situ monitoring programs, it is also difficult to estimate the size, duration, extent and historical context of these plumes. Satellite observing systems, in contrast, offer a means by which these plumes can be monitored and compared to previous events. As such, turbidity plumes visible in Landsat 8 and MODIS Aqua imagery were first manually outlined, and then refined (for MODIS only) using anomaly and normalized anomaly thresholds determined from pre-dredging data. Local environmental conditions were also considered and used to determine dates for which elevated reflectance data might be expected in the absence of dredging. In total, the spatial extent of all turbidity plumes observed from November 2013 to April 2015 was between 127 and 228 km², at least 5 times that for January – October 2013. Furthermore, the frequency of observed plumes in images increased from 23% to 84% after dredging began. Coral areas were particularly affected after dredging began, with over 11 km² of coral area being within plumes on an average of 16% of images (maximum 39%). Temporal differences in location, severity, and size were also observed. Together, these results highlight widespread turbidity plumes associated with the Port of Miami dredging activities, which may cause large adverse effects on local coral communities. The approaches developed in this work, in particular the focus on historical norms after considering all perturbation factors, may be included in monitoring and assessment of this and future dredging activities, especially where fragile marine ecosystems may be impacted.

© 2015 Elsevier Inc. All rights reserved.

1. Introduction

1.1. Background on remote sensing of sediment plumes

Dredging activities are a regular component of port building and maintenance, as dimensions of the waterways must exceed that of the ship traffic. Since the completion of the Panama Canal in 1914, the length, width, and draft of ships crossing through the Canal have been restricted based on the dimensions of the locks (ship size limits are termed 'Panamax'). The Panama Canal Expansion project (estimated completion in 2016) will double the current Canal capacity through the addition of a third set of locks which can accommodate larger ship sizes (termed 'New Panamax'; Mulligan & Lombardo, 2011). As a result of this change, many ports throughout the world (including the Port of Miami) have been, or are slated to be, expanded via dredging.

In the process of extracting and relocating bedrock and sediment, dredging activities are expected to cause reductions in water clarity and increased particle concentrations. Specifically, sediment spillage can occur as the drill head cuts into the substrate and the resulting sediment-laden water is pumped to a transport barge (Fig. 1a). Subsequent dewatering of the transport barge (decanting water after settlement of sediment within the barge) can further release unsettled fine sediments (Fig. 1b). Finally, potential leakage during transport of the sediment and eventual disposal (e.g., at an offshore location or beach for renourishment) also result in water clarity decreases.

For coastal areas, turbidity (or suspended sediment concentration) can also be influenced by several environmental parameters, including wind (e.g., resuspension), tidal forcing (e.g., ebb-tidal plume), rainfall and subsequent riverine outflow, and extreme weather events (e.g., hurricanes). The relationships between these environmental conditions and natural turbidity events are also spatially variable (e.g., according to distance from inlet). As such, differentiating dredging-related turbidity and that caused by these natural environmental conditions requires long term analyses that account for this spatial

* Corresponding author.

E-mail address: bbarnes4@mail.usf.edu (B.B. Barnes).

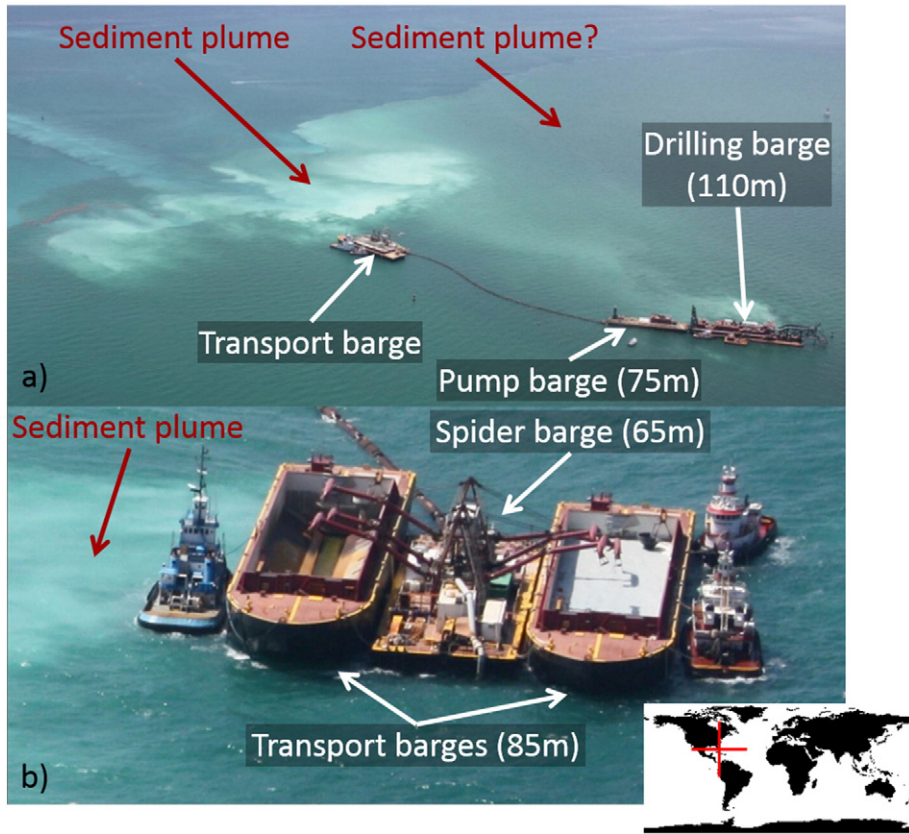


Fig. 1. Dredging activity and resulting sediment plumes. Images taken on 25 June 2014. Approximate lengths of the barges are listed for scale. Drilling barge location is approximately 25.758 N, 80.109 W. Photo Credit: Daniel Kipnis.

variability due to multiple factors. Due to the expense of sampling effort and lack of adequate (historical) baseline data, capturing the extent (size, duration, and intensity) of sediment plumes is therefore difficult using in situ data (Wang, Lu, Liew, & Zhou, 2009).

High-to-moderate resolution satellite imagery (e.g., Landsat at 30-m resolution) can provide a clear outline of bright sediments (Fig. 2, solid outline). Furthermore, several algorithms have been developed to convert Landsat reflectance data to turbidity in a variety of environments, including lakes and reservoirs (Hadjimitsis, Hadjimitsis, Clayton, & Clarke, 2006; Lathrop, Lillesand, & Yandell, 1991; Ritchie & Cooper, 1988), rivers (Islam, Yamaguchi, & Ogawa, 2001; Wang et al., 2009), wetlands waters (Mertes, Smith, & Adams, 1993), and coral lagoons (Ouillon, Douillet, & Andréfouët, 2004). However, Landsat instruments have low repeat sampling frequency (16 days), resulting in relatively

large temporal gaps between measurements. Low repeat sampling frequency also hinders assessment of turbidity events relative to historical context, as pre-event baseline conditions (e.g., climatologies) are difficult to establish. As such, it can be difficult to distinguish between moderate turbidity events and historically normal conditions (e.g., Fig. 2 dotted outline). Furthermore, prior to Landsat 8 (which carries the Operational Land Imager; OLI; launched February 2013), atmospheric correction of Landsat data required ancillary atmospheric data (e.g., Hu, Muller-Karger, Andrefouët, & Carder, 2001), dark pixel assumptions (e.g., Lathrop et al., 1991; Palandro et al., 2008) or pixel aggregation with resulting loss of spatial resolution (e.g., Barnes et al., 2014). Such atmospheric correction (and associated cloud detection) is required for quantitative assessment of spatial and temporal variation, especially for water targets.

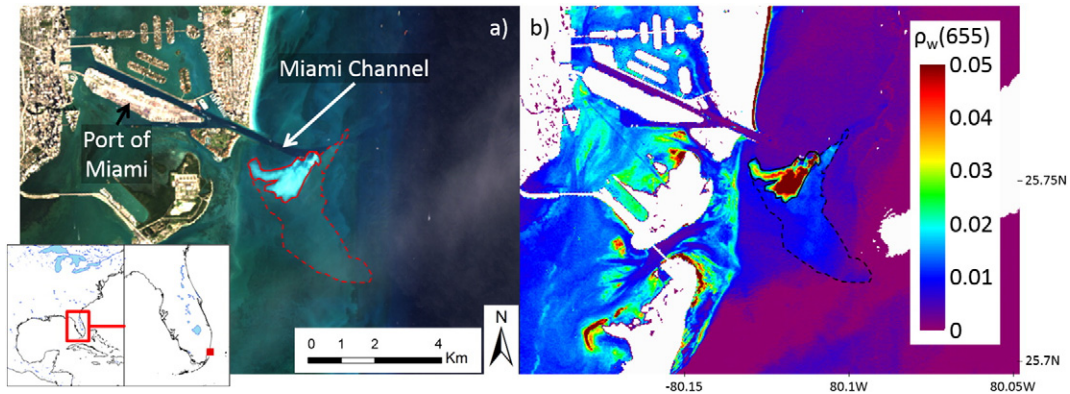


Fig. 2. Landsat8 (a) true color, and (b) $\rho_w(655)$ (dimensionless) imagery from 18 January, 2014. Solid outlines show clear dredging plume, while dotted outline shows area potentially affected by dredging-related turbidity.

Moderate resolution satellite data [e.g., that from the National Aeronautics and Space Administration (NASA) Moderate Resolution Imaging Spectroradiometer (MODIS), with its 250-m bands], can also be used to assess dredging-related plumes (He, Hu, & Hu, 2014). The approximately daily repeat sampling, in combination with an instrument that has been providing science quality data for over a decade, can offer a long-term perspective on the size, duration, and intensity of events. For MODIS, several algorithms have been developed to derive turbidity or concentrations of suspended particulate matter [SPM, also called total suspended matter (TSM) or total suspended solids (TSS)] from remote sensing reflectance (R_{rs}) data (Matthews, 2011). These algorithms generally use an empirical relationship between measured turbidity and either a single red band (Dogliotti, Ruddick, Nechad, Doxaran, & Knaeps, 2015; Feng, Hu, Chen, Tian, & Chen, 2012; He et al., 2014; Hu et al., 2004; Miller & McKee, 2004; Petus et al., 2010) or a ratio between red and green bands (Doxaran, Cherukuru, & Lavender, 2006). For the former approach, simple linear correlations often indicate strong relationships between red band reflectance and turbidity ($r^2 > 0.82$; Matthews, 2011). As such, for this work we have used red band reflectance as a proxy for turbidity.

1.2. Study area and objectives

The Port of Miami (also called 'PortMiami') is one of the busiest ports in the southeastern United States, servicing approximately 5 million cruise ship passengers and 8 million tons of cargo in 2014 (miamidade.gov/portmiami, accessed 15 May 2015). To accommodate New Panamax sized ships, the Port Miami Deep Dredge (PMDD) project proposed to dredge $3.8\text{--}4.6 \times 10^6 \text{ m}^3$ of material from Miami Harbor, increasing the channel depths by 2–3 m and widening turning basins up to 100 m (FDEP, 2012). Construction began in November 2013, and was completed in August 2015. In general, dredging activities began offshore and progressed towards the Port of Miami, with major offshore dredging activities completed by December 2014.

The City of Miami is also a popular tourist destination, with approximately 14.5 million overnight visitors spending over \$24 billion in 2014 (Sampson, 2015). Among the main draws to the region are the beaches and marine life (e.g., coral reefs, seagrass beds, recreational fisheries, Fig. 3). Corals, in particular, were of great concern in permitting the PMDD project, as seven local species (including *Acropora palmata* and *Acropora cervicornis*) are listed as threatened by the Endangered Species Act (US Department of Commerce, 2014). Sedimentation, sediment scour, and light limitation resulting from turbidity events can all directly harm corals (Erftemeijer, Riegl, Hoeksema, & Todd, 2012; Philipp & Fabricius, 2003; but see Goreau et al., 2000), and may further increase disease prevalence (Pollock et al., 2014). *A. palmata* (elkhorn) corals are among the most susceptible to sedimentation, while *A. cervicornis* (staghorn) corals are particularly sensitive to turbidity-driven shading (Rogers, 1990). As such, the PMDD permit required elkhorn and staghorn colonies within the anticipated indirect impact area (150 m surrounding the channel) to be relocated (FDEP, 2012). Nevertheless, the Florida Department of Environmental Protection (FDEP) and others have documented sedimentation (up to 14 cm deep) causing mortality to corals (including *A. cervicornis*), both within and beyond the indirect impact area (FDEP, 2014; NOAA NMFS 2015; Dial Cordy and Associates 2015).

Given the large scale and potential environmental consequences of the Port of Miami dredging activities and the difficulty in assessing such consequences using in situ data alone, the objective of this research was to use satellite-derived R_{rs} to capture the size, duration, extent, and historical context of turbidity events related to the PMDD project. As certain characteristics of the study region present barriers to appropriate application of traditional turbidity algorithms (particularly benthic reflectance contributions to the measured radiance), we present here a novel approach to turbidity assessment based on $R_{rs}(667)$ anomaly detection, manual outlining and threshold-based delineation, and concurrent environmental conditions.

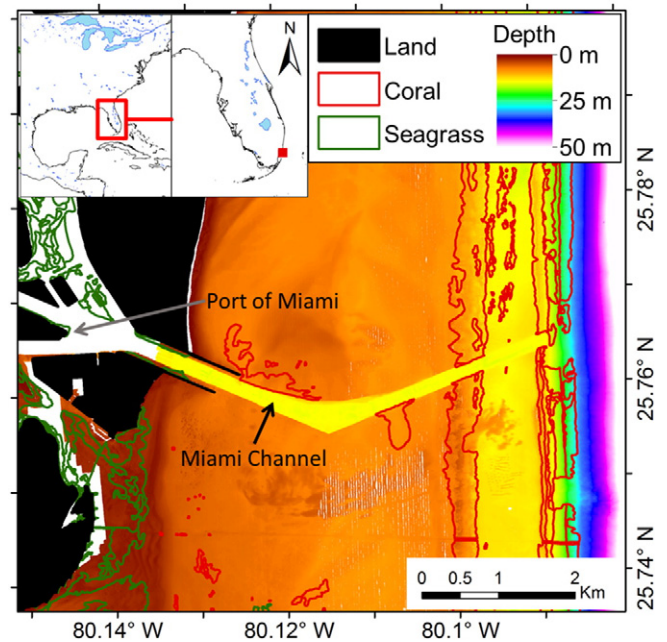


Fig. 3. Bathymetry of the study region, with benthic habitat classification of corals (red) and seagrasses (green) outlined. Bathymetry data from NOAA National Geophysical Data Center (NGDC) Hydrographic Surveys H11870, H11869, H11897, and H11898. Coral and seagrass distribution from Florida Fish and Wildlife Research Institute (FWRI) Unified Florida Coral Reef Tract Map (<http://ocean.floridamarine.org/IntegratedReefMap/UnifiedReefTract.htm>).

2. Methods

From a remote sensing perspective, waters in this study area range from optically shallow to optically deep, with boundaries between these different waters changing in both space and time. For optically shallow waters (where benthic reflectance can influence the R_{rs} measured from an above-water radiometer), single red band approaches to estimate turbidity from R_{rs} data are generally preferred because the high absorption coefficient of water in red wavelengths makes the algorithm less susceptible to benthic interference (He et al., 2014). Nevertheless, for much of the shallow water in the study area, red band reflectance is correlated to water depth, indicating that the benthic signal remains (see Barnes et al., 2013). As such, assuming temporally constant albedo, turbidity assessment in this region requires an approach based on detection of anomalies from established climatologies. Although MODIS band 1 data [$R_{rs}(645)$] has been previously used to estimate turbidity (Feng et al., 2012; He et al., 2014; Miller & McKee, 2004; Petus et al., 2010), climatologies calculated using $R_{rs}(645)$ data [as well as $R_{rs}(859)$] in this region suffered from significant speckling (potentially due to insufficient cloud masking), confounding anomaly-based detection methods.

2.1. Satellite data acquisition and processing

All MODIS Aqua Level 1A data from July 2002 – March 2015 were downloaded from NASA Goddard Space Flight Center (GSFC; oceancolor.gsfc.nasa.gov). These data were processed to R_{rs} and Rayleigh corrected reflectance (R_{rc}) at 250 m resolution using SeaDAS (version 7.0.2; Baith, Lindsay, Fu, & McClain, 2001) and custom programs. For R_{rs} in the ocean color bands, this required subsampling (linear interpolation) from 1 km data, accomplished via SeaDAS. R_{rc} data were combined to create true color RGB images using a logarithmic stretch (from 0 to 0.01) for each of the 645, 555, and 469 nm bands (red, green, and blue, respectively). In the creation of these images, the 500 m resolution bands (469 and 555 nm) were sharpened using the 645 nm (red) band, whereby the pixel

specific ratio between the red band data at full resolution (250 m) and that data spatially averaged (to 500 m resolution) was applied to the other two bands.

For R_{rs} data, standard SeaDAS Level 2 processing flags (Patt et al., 2003) were used to identify questionable pixels (e.g., cloud contaminated, land, etc.; see Barnes & Hu, 2015 for complete list), which were removed from all further analyses. All R_{rs} and R_{rc} data were mapped to an Equidistant Cylindrical projection. For the time period from 2002 to 2012 (the 'baseline' period), 31-day moving mean and standard deviation climatologies were calculated for MODIS $R_{rs}(667)$. Mean climatologies were calculated as the pixel specific sum of $R_{rs}(667)$ within the each 31 day span, divided by the pixel specific number of valid satellite measurements. Standard deviation climatologies represent the pixel- and span- specific standard deviations about these means. For MODIS R_{rs} data from January 2013–22 March 2015 ('test' period), anomaly [daily $R_{rs}(667)$ – corresponding mean climatology] and normalized anomaly (anomaly/ corresponding standard deviation climatology) values were calculated. For the test period, $R_{rs}(667)$ anomaly data were scaled using a linear stretch from -0.00024 to 0.0021 sr^{-1} (2% and 98% thresholds for all images) and stored as.PNG images. Normalized anomaly data were processed similarly, but with scaling from -2 to 2 standard deviations.

All Landsat 8 scenes in the study area (row 15, path 42) were downloaded from the United States Geological Survey (USGS; earthexplorer.usgs.gov). These data were processed using ACOLITE software (developed by the Royal Belgian Institute of Natural Sciences), using both the NIR and SWIR atmospheric correction algorithms (Vanhellemont & Ruddick, 2014, 2015). Data processed with both the NIR and SWIR algorithms showed benthic contamination in this scene, however benthic effects and other artifacts were generally less for data processed using the former. As such, the NIR-processed data was used for all subsequent analyses. True color RGB images were created with linear scaling of each band from 0 to 0.15. Red band water leaving reflectance [$\rho_w(655)$; $\rho_w = R_{rs} \times \pi$; dimensionless] was also extracted and stored as.PNG images with linear stretch from 0 to 0.05.

2.2. Environmental data

Wind data from 2002 to 2015 were downloaded from the National Oceanic and Atmospheric Association (NOAA) National Data Buoy Center (NDBC; ndbc.noaa.gov) station at Fowey Rocks, FL (FWYF1). Anomalous data were removed (individual measurements more than 5 m s^{-1} from a 24 h running mean), and vector math was used to calculate the average daily wind speed and direction. Note that this station ceased transmitting data on 10 January 2015. Tide data (time and water level relative to MLLW at each low tide) were downloaded from the NOAA station at Virginia Key, FL (station 8723214; tidesandcurrents.noaa.gov). Rainfall totals were obtained from the NOAA National Climatic Data Center (NCDC) station at the Miami International Airport (station 509370; ncdc.noaa.gov). Finally, canal discharge data was downloaded from the USGS station 02289500 (Tamiami Canal near Coral Gables, FL; waterdata.usgs.gov). Although gaps exist in many of these time series, these data are from the nearest relevant station to the study area with continuous (or nearly continuous) records since 2002.

2.3. Plume delineation

2.3.1. Manual outlining of the plume region

Manual outlining was performed using a custom IDL-based graphical user interface (GUI) which simultaneously displayed corresponding RGB, anomaly, and normalized anomaly.PNG images. Contiguous areas where turbidity plumes were apparent in the RGB and also seen in either the anomaly or normalized anomaly images were manually outlined. Plumes apparent in RGBs but where valid $R_{rs}(667)$ data was unavailable (usually near the MODIS scan edge or underneath atmospheric haze), were also outlined and termed 'RGB-only outlines'.

Images where no detectable plume was observed were also noted. Similarly, for Landsat, RGB and $\rho_w(655)$.PNGs were used to manually outline plumes using a custom GUI. The areal extent of these Landsat plumes was calculated by multiplying the number of outlined pixels by $(1/958) \text{ km}^2$. Note that throughout this work, the term 'plume' is used to describe anomalous turbidity conditions likely caused by dredging activities. Nevertheless, identified plumes or anomalies may also be capturing events wholly or partially resulting from natural environmental conditions.

2.3.2. Reflectance thresholds

The manually outlined plumes show turbidity events which are both dredging- and non-dredging related. To distinguish between these conditions, a time series of the mean MODIS-derived $R_{rs}(667)$ for a 2 km 'virtual station' most frequently included in the outlined plume regions was extracted for 2002–2014. This virtual station was centered at 25.759 N, 80.092 W. For this time series, records with fewer than 5 (of 64) data points or standard deviation = 0 (i.e., from single MODIS measurement, extrapolated) were removed from further analysis. Wind, tide, rainfall, and canal discharge data associated with each measurement in the MODIS time series were determined. Data were plotted to qualitatively determine which parameters were associated with elevated $R_{rs}(667)$. A series of rules (or thresholds) was established to differentiate environmental data which were typically associated with elevated $R_{rs}(667)$ in non-dredging conditions. These thresholds were determined through visual inspection of the data, but were restricted to relationships expected for coastal marine systems. $R_{rs}(667)$ data with corresponding environmental conditions which favored elevated $R_{rs}(667)$ were flagged and excluded from further analysis. The 90th percentile for the remaining pre-dredging data was calculated and considered to be the threshold for defining elevated $R_{rs}(667)$ during normal environmental conditions and in the absence of dredging. Throughout this work, Student's *t*-tests were performed to assess differences between groups. In cases where Lilliefors tests and Bartlett's tests indicated departures from normality or homoscedasticity, respectively, Wilcoxon rank sum tests were employed instead.

2.3.3. Refining plume delineations

The anomaly and normalized anomaly values associated with the post-dredging data above the $R_{rs}(667)$ threshold were extracted. From these data, the 10th percentile for each parameter was calculated. These values were considered thresholds for detecting anomalous $R_{rs}(667)$ conditions, and were thus applied to pixels within the delineated plumes. Specifically, all pixels within manually outlined plumes were determined to be 'threshold delineated' (anomaly or normalized anomaly data above the threshold), 'incorrectly delineated' (anomaly and normalized anomaly data below the thresholds), or without valid $R_{rs}(667)$ data. For each plume, the percentage of threshold delineated pixels relative to all outlined pixels with valid $R_{rs}(667)$ data was calculated (i.e., 'success rate'). To quantify the spatial area of MODIS data, the number of pixels was multiplied by $(1/16 \text{ km}^2)$. To estimate the total plume area, the area of the threshold delineated plumes was added to the area of pixels without valid $R_{rs}(667)$ data times the image-specific success rate. For RGB-only outlines, the area of the manually outlined plume was multiplied by the study-wide success rate (i.e., for all delineations combined).

3. Results

3.1. Plume delineation

3.1.1. Manual plume outlining

In total, of 808 MODIS passes between 1 Jan. 2013 and 22 Mar. 2015, 186 included sufficient coverage and data quality to allow for 1) determination of plume presence/absence and 2) plume outlining. Of these, 66 such determinations were made using RGB-only data, and 129 showed

evidence of a plume. Fig. 4 shows a time series of manually outlined MODIS plumes for the month from 11 Jan. 2014 to 10 Feb. 2014. For Landsat, of the 37 scenes between 2 April 2013 and 26 March 2015, 21 had sufficient coverage, with a plume visible in 14. Six determinations were made using RGB-only data.

3.1.2. Reflectance thresholds

Before filtering for environmental conditions, the 90th percentile for the pre-dredging $R_{rs}(667)$ time series at the virtual station was 0.0013 sr^{-1} (Fig. 5a). In contrast, only 71% of post-dredging data were below this mark. A two-sample *t*-test indicated that the pre- and post-dredging datasets were statistically different ($p < 0.001$). Nevertheless, ancillary environmental data was used to parse out conditions which typically foster elevated $R_{rs}(667)$ in this time series.

Plotting wind vectors for the pre-dredging time period against MODIS $R_{rs}(667)$ shows clear increases in $R_{rs}(667)$ according to wind speed, but not wind direction (Fig. 6a). Once dredging begins, this relationship is not apparent (Fig. 6b). Similarly, higher $R_{rs}(667)$ values were observed when the MODIS measurements occurred temporally close to low tide (i.e., late ebb tide or early flood tide), while tidal height at low tide (i.e., spring-neap effects) did not show a clear relationship with $R_{rs}(667)$ (Fig. 7). Lagged correlation coefficients were calculated between the rainfall and outflow datasets to assess the duration of time between rainfall and subsequent outflow. While none of these tests showed strong correlation, the highest coefficient of determination ($R^2 = 0.041$) indicated a one-day lag best described the relationship between rainfall and outflow. $R_{rs}(667)$ plotted against the one-day lagged rainfall data and the canal discharge data (similar to Figs. 6 and 7), indicated elevated $R_{rs}(667)$ coincident with the highest rainfall and discharge records. Table 1 shows the threshold environmental conditions which were found to be typically associated with high $R_{rs}(667)$.

Combining these thresholds, Fig. 8a shows the exclusion criteria for data according to environmental conditions. Data above the dotted line (considering tidal stage and windspeed) or marked with plus symbol (high rainfall or high discharge) are considered favorable for high $R_{rs}(667)$ and excluded from further analysis. Throughout this manuscript, the term ‘environmental flag’ is used to define dates for which

the environmental conditions exceeded these thresholds. Note that these thresholds exclude 25% of all pre-dredging data, but 65% of all pre-dredging data with high $R_{rs}(667)$ (Table 1). The accuracy of this determination was 26% (Table 1). For post-dredging data, a smaller proportion of the high $R_{rs}(667)$ data was excluded using these thresholds (19%, Fig. 8b). However, 26% of the remaining post-dredging data has high $R_{rs}(667)$, compared to just 5% for pre-dredging data.

Applying these thresholds to the entire time series (Fig. 5b), a much clearer increase in $R_{rs}(667)$ can be observed, associated with the start of the dredging. Indeed the 90th percentile for this filtered pre-dredging data was 0.0009 sr^{-1} . In contrast, only 62% of the post-dredging data showed $R_{rs}(667)$ below this threshold. Again, a two-sample *t*-test indicated that the pre- and post-dredging datasets are statistically different. From this threshold, the 10th percentile for the corresponding anomaly and normalized anomaly values were determined (0.0003 sr^{-1} and 0.34 standard deviations, respectively) and used to identify ‘threshold delineated’ pixels within manually outlined plumes.

3.1.3. Refined plume delineations

Within manually outlined plume regions, the percentage of data without valid $R_{rs}(667)$ ranged from 0 to 91% (average = 49%). As such, no determination based on threshold anomaly and normalized anomaly values could be made on approximately half of the manually outlined pixels. For the remaining pixels, the success rate for manual outlines was 67% for all delineations combined, while image-specific success rates ranged from 0 to 100% (average = 56%).

Fig. 9 shows spatial frequency maps of the manually outlined and threshold delineated plumes. Very few plumes were detected prior to dredging activities commencing in November 2013 (Fig. 9, left column). Not surprisingly, plumes were most often seen immediately offshore from the Port of Miami mouth. Winter and spring 2014 showed the greatest frequency of affected pixels, while plumes were less frequent in summer and autumn 2014. This decrease in extent and severity may result from dredging activities beginning offshore and moving inshore.

Threshold delineated plumes have smaller range and frequency than the manually outlined plumes (Fig. 9), due to the requirement for valid

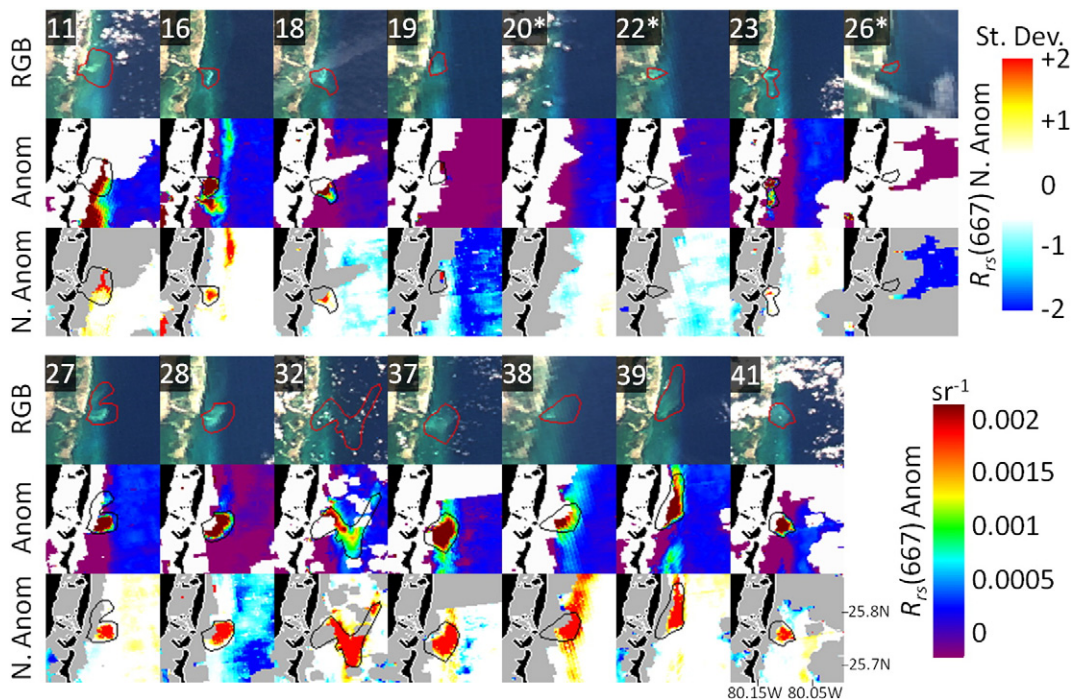


Fig. 4. Time series demonstrating manual plume outlining on MODIS true color RGB (rows 1 & 4), anomaly of $R_{rs}(667)$ (sr^{-1}) (Anom, rows 2 & 5), and normalized $R_{rs}(667)$ anomaly (N. Anom, rows 3 & 6) for Julian days in 2014 listed in top left corners of RGB images. Dates with asterisks indicate days where outlining was performed using RGB-only data.

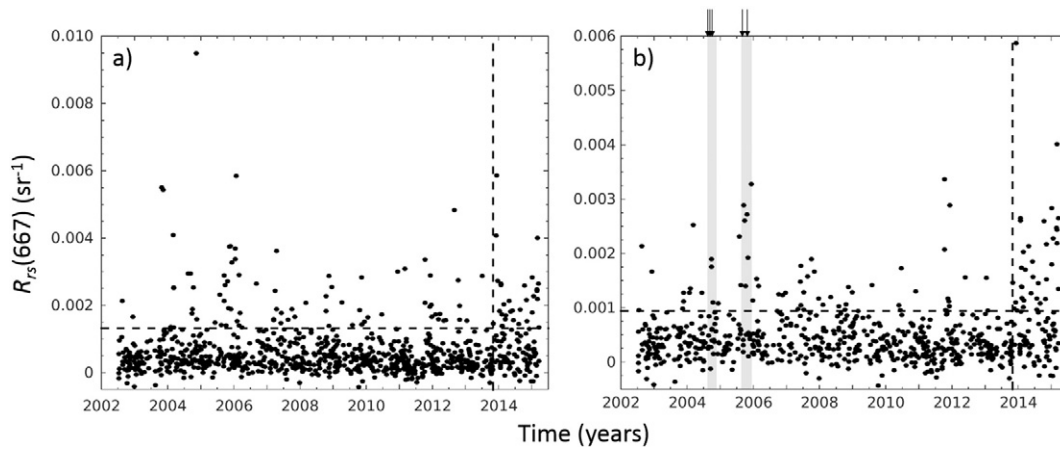


Fig. 5. a) MODIS time series of mean $R_{rs}(667)$ (sr^{-1}) for the virtual station. Same data shown in (b) after removing measurements identified by any of the environmental quality tests. Horizontal dotted lines show 90th percentile for pre-dredging data [0.0013 and 0.0009 sr^{-1} in (a) and (b), respectively]. Vertical dotted line marks beginning of dredging (Nov 2013). Arrows indicate hurricane landfall within 250 km. Gray bars highlight 2 months after each landfall.

$R_{rs}(667)$ data, as well as overestimation of the manual outlining. As a result of the former, these plumes were concentrated further offshore [nearshore $R_{rs}(667)$ data were more likely to be identified by the L2 processing flags, see Fig. 4]. Nevertheless, large differences in plume size and frequency were observed pre- and post-dredging, regardless of the plume detection method.

3.2. Plume extent and duration

Fig. 10 combines the MODIS and Landsat data to show the estimated areal extent of the plumes as a function of time. For this representation, delineations made using RGB-only images, as well as instances where high $R_{rs}(667)$ would be expected during normal (non-dredging) conditions ('environmental flag'), are separately indicated. A clear increase in the size and frequency of plumes is visible after the start of dredging activities. Prior to the start of dredging, sediment plumes were identified on 10 (of 44) images. For two of those delineations, the threshold tests indicated that none of the pixels was anomalous, while another 6

delineations were on environmentally flagged dates. Indeed, a two-tailed Wilcoxon rank sum test for pre-dredging data indicated that plume area on environmentally flagged dates was significantly different (larger) than that on dates where environmental conditions did not favor high $R_{rs}(667)$ (Z-statistic = 2.4, $p = 0.016$).

Of the 117 delineations between November 2013 and December 2014, one third were from dates identified by the environmental flag. In contrast to the pre-dredging data, plume area for these post-dredging delineations was not significantly different based on the environmental flag (two-tailed Wilcoxon rank sum test, Z-statistic = 0.6, $p = 0.54$). Note that environmental flag determination was not made for dates in 2015 due to the lack of wind speed data.

3.3. Impact on coral areas

Pixels with coral cover were among the most frequently affected by the turbidity plumes. For both the manual outlines and threshold delineations, the area of corals under influence of the plumes nearly doubled

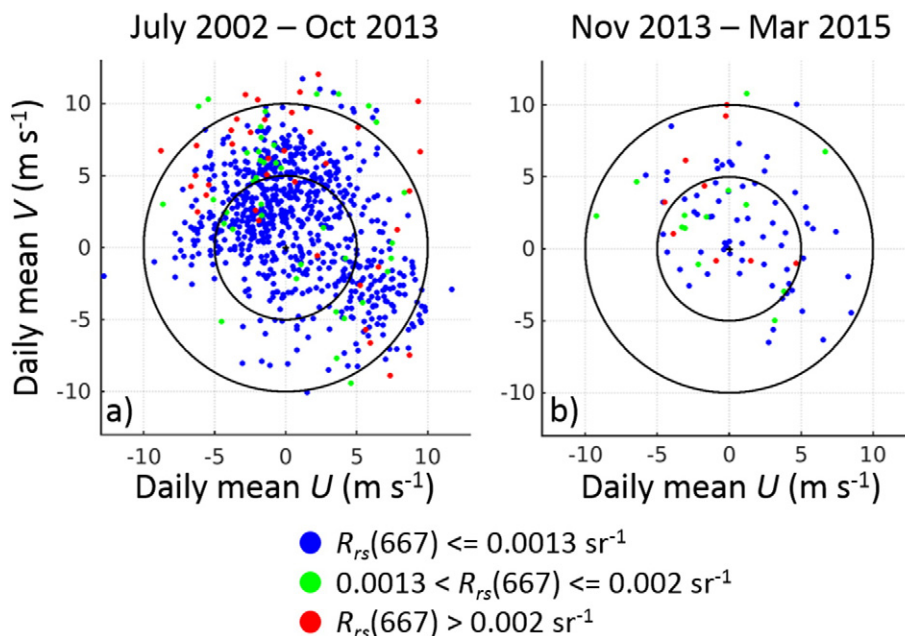


Fig. 6. Daily mean wind vectors (U and V components, $m s^{-1}$) corresponding to MODIS-derived $R_{rs}(667)$ (sr^{-1}) for the virtual station (a) before and (b) after dredging began. Point color indicates categorical representation of $R_{rs}(667)$ data (green = 90th percentile, red = 95th percentile). Concentric circles indicate wind speeds of 5 and 10 $m s^{-1}$.

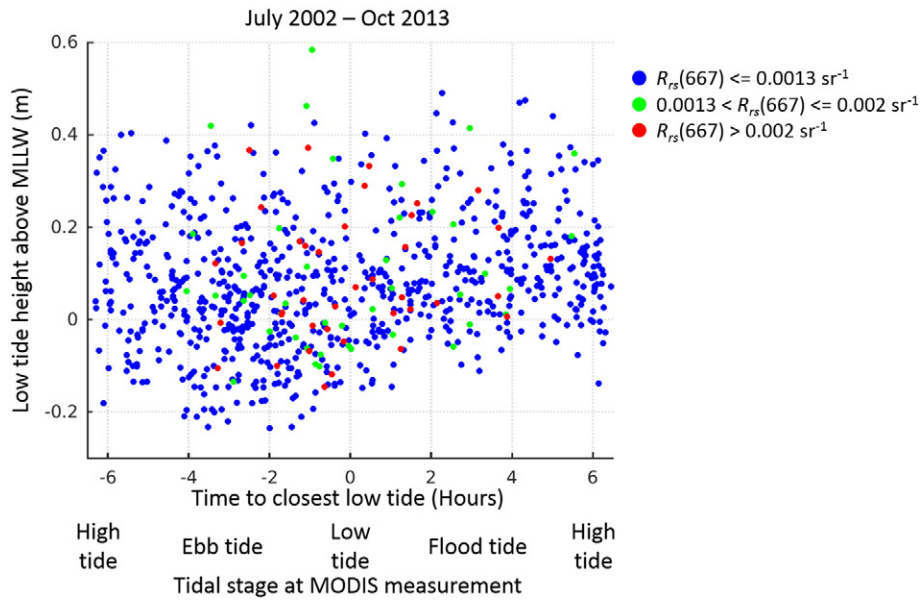


Fig. 7. Daily mean tidal condition [time to closest low tide (hours) and low tide level (m above MLLW)] corresponding to MODIS-derived $R_{rs}(667)$ (sr^{-1}) for the virtual turbidity station before dredging began. Point color indicates categorical representation of $R_{rs}(667)$ data (green = 90th percentile, red = 95th percentile).

after dredging began (Table 2). Furthermore, the average and maximum frequency of these impacts on pixels with coral cover also nearly doubled, meaning twice the coral area was being impacted twice as often. Conditions were most extreme in winter 2014, when some coral pixels were within threshold delineated plumes on 57% of images (88% for manually outlined plumes).

The manually outlined plumes represent the largest visible extent of plumes in these images, regardless of corroborating $R_{rs}(667)$ data, while the threshold delineated plumes indicate the minimum extent. Together, these results highlight a large and sustained effect of the dredging project on local turbidity. The overall affected area was between 127 and 228 km^2 (according to the threshold delineated and manually outlined plumes, respectively), although nearly a third of that region was affected only once. This region of impact is approximately 5 times that observed for plumes seen prior to dredging (18–46 km^2). Furthermore, the frequency of plume occurrence in images nearly quadrupled, from 23% to 84%.

4. Discussion

Coastal oceans are dynamic, where ocean properties may change faster than in deep, open oceans away from land. As such, the size, shape, and extent of the plumes were quite variable. Measured by MODIS, plume area varied by tens of km^2 over the course of several days. While some of this can be attributed to measurement uncertainties (see Section 4.2), there is undoubtedly large day-to-day variation in plume extent and severity. Indeed, even same-day RGB images from Landast and MODIS (Fig. 11) show large deviations in the observable

plumes. The time difference between these images is just over 2.5 h, as Landsat typically overpasses this region at 15:50 UTC, while the MODIS Aqua overpass on those days is at 18:25 UTC. This variability could result from strong local currents (both tidal and non-tidal) advecting and dispersing sediments, and/or rapid settlement of suspended sediments. Bokuniewicz and Gordon (1980) recorded descent speeds for dredging spoil as fast as 1.5 m s^{-1} , with lateral advection modulated by current velocity. No such characterization of sediment settlement velocities has been reported for this dredging event. However, reports of coral smothering (FDEP, 2014) indicate that settlement of particles explains least a portion of the day-to-day plume variability.

4.1. Impact of environmental conditions on plumes

The time series in Fig. 5 shows increased frequency of high $R_{rs}(667)$ measurements after dredging began. However, even after removing data points for which environmental conditions favored high $R_{rs}(667)$, high $R_{rs}(667)$ data remain within the pre-dredging time series (Fig. 5b). These outliers were investigated in further detail. Tropical storms and hurricanes impact this region nearly every year, either through direct landfalls or storm paths close enough to expose the region to storm surge or severe weather. The effect of such storms can clearly be seen in true color imagery of the region (see Fig. 12a,b). Hurricane activity in 2004 and 2005 was anomalous, as southern Florida experienced 5 hurricane landfalls (Charley – August 2004, Frances – September 2004, Jeanne – September 2004, Katrina – August 2005, Wilma – October 2005). In comparison, zero hurricanes made landfall in southern Florida for the rest of this time series. Indeed, fully 15% of

Table 1
Threshold values for environmental conditions associated with elevated $R_{rs}(667)$.

	Number of pre-dredging $R_{rs}(667)$ measurements (% of total)	Number of pre-dredging $R_{rs}(667)$ measurements above 90th percentile (%)	Number of post-dredging $R_{rs}(667)$ measurements above 90th percentile (%)
All data	819 (100%)	82 (100%)	31 (100%)
Windspeed $>9.7 \text{ m s}^{-1}$	47 (6%)	17 (21%)	2 (6%)
MODIS measurement within 2 h of low tide AND windspeed $>5 \text{ m s}^{-1}$	149 (19%)	42 (51%)	5 (16%)
One-day lag rainfall $>45 \text{ mm}$ (1.8 in.)	5 (1%)	1 (1%)	0 (0%)
Discharge $>11.19 \text{ m}^3 \text{ s}^{-1}$ (395 cu. feet s^{-1})	11 (1%)	5 (6%)	0 (0%)
Combined flags	204 (25%)	53 (65%)	6 (19%)

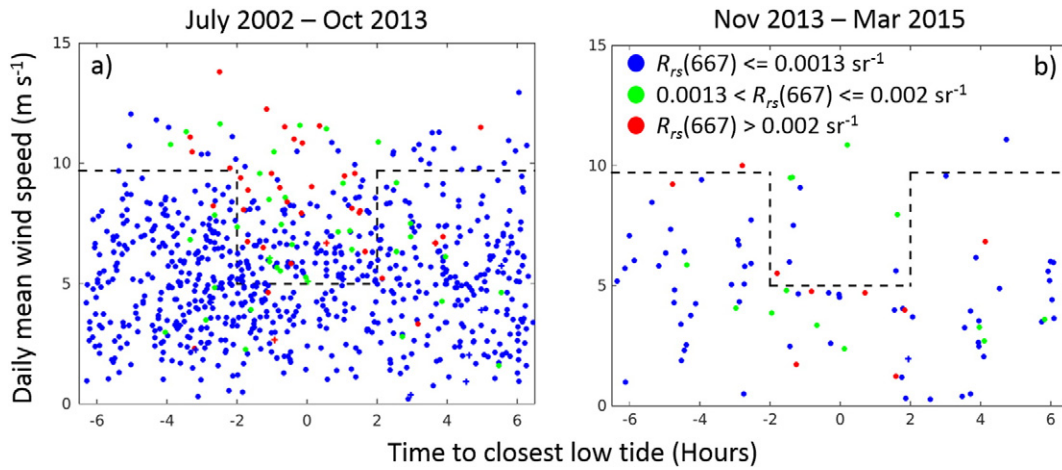


Fig. 8. Daily mean tidal condition (time to closest low tide, hours) and daily mean wind speed (m s^{-1}) corresponding to MODIS-derived $R_{rs}(667)$ (sr^{-1}) for the virtual turbidity station (a) before and (b) after dredging began. Point color indicates categorical representation of $R_{rs}(667)$ data (green = 90th percentile, red = 95th percentile). Data identified as high rainfall or high outflow marked as '+'.

the pre-dredging outliers in Fig. 5b fall within two months after these 5 storms.

Mesoscale eddies were associated with nearly all of the remaining pre-dredging outliers in Fig. 5b. Typically very strong northward currents (associated with the Gulf Stream) are immediately adjacent to this region. However, eddies can propagate along the southeastern coast of Florida (Kourafalou & Kang, 2012; Lee, 1975). As such eddies pass the region, shifting current patterns to offshore (eastward) could foster increased turbidity, which is apparent in CI imagery (Hu, 2011). Note that the eddy seen in Fig. 12b is much larger and more apparent in true color RGB images than is typical since this image immediately follows a hurricane landfall. While historical current vector data from this region is available (e.g., from the US Navy Department of Defense HYCOM model; Chassignet et al., 2007), the spatial resolution is coarse. As such, the modeled current vector signal is dominated by the fast moving Gulf Stream, and smaller eddies are not well represented. Finally, widespread high $R_{rs}(667)$ was also occasionally seen for all shallow waters without apparent etiology (see Fig. 4 anomaly image on Julian Day 11). The reason is unclear, but these few cases would not impact the overall interpretation of the before-after changes in relation to the dredging.

The pre- and post-dredging $R_{rs}(667)$ time series were significantly different even before removal of points based on environmental conditions (Fig. 5a). Nevertheless, the retrospective analysis of the conditions typically associated with elevated $R_{rs}(667)$ (Sections 2.3.2, 3.1.2) is important not only for placing the plume events in historical context, but also for providing a framework through which to interpret the results. The before-after changes are also enhanced after ruling out the plume

events caused by factors other than dredging. For example, during the post-hurricane time period (two months after each landfall), only 26% of data points fall outside the pre-dredging 90th $R_{rs}(667)$ percentile, compared to 38% for the 17 months of dredging activity. Thus, according to this analysis, impacts from the dredging activity in this particular region were at least on par with that following hurricane landfalls, but spanning nearly 1.5 years. Also, even though 10 pre-dredging images in 2013 showed evidence of a plume (Fig. 10), all but two were on dates that environmental conditions favored high $R_{rs}(667)$. This amounts to plumes visible on only 8% of pre-dredging images during 'normal' environmental conditions, compared to 74% of images from November 2013 to December 2014 (lack of wind data precludes environmental flag determination after January 2015).

Shi, Wang, and Jiang (2011, 2013) noted significant variation in TSM according to spring-neap tidal effects (in the same order as seasonal variations) in the Bohai Sea, Yellow Sea, East China Sea, and portions of the Chesapeake Bay. However, the current study indicated no trends in $R_{rs}(667)$ according to tidal height (Fig. 7). While the tidal influence is clear in aggregated datasets and climatologies (see Shi et al., 2011, 2013), for individual images in this study region the tidal influence is more complex, and more strongly dependent on the time of the satellite measurement relative to the tidal stage. Moreover, other factors (especially wind speed, Fig. 6) also greatly influence the local turbidity, potentially obscuring large-scale variation in turbidity according to spring-neap tidal effects.

It is important to note that although the thresholds used to define the environmental flag were defined rather subjectively, the presented results (especially the pre- and post-dredging comparisons) would not

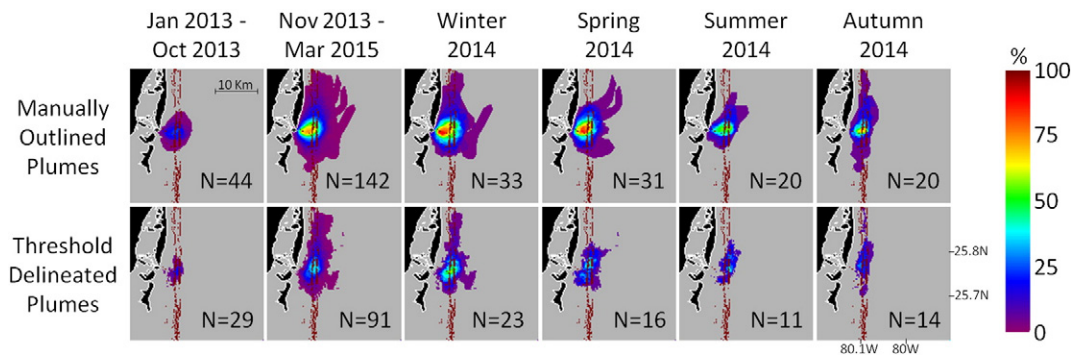


Fig. 9. Spatial frequency maps (as percentage of maximum) showing extent and frequency of (top row) manually outlined plumes and (bottom row) threshold delineated plumes for time ranges indicated. Pixels with coral cover indicated in red. Maximum number of images are indicated in the bottom right of each panel.

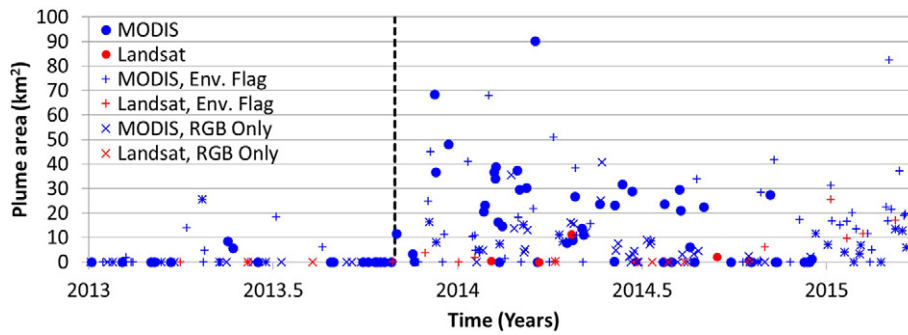


Fig. 10. Estimated area (km²) of plumes determined from MODIS (blue) and Landsat (red). Data with reduced certainty due to environmental conditions favoring high $R_{rs}(667)$ (Env. Flag) and/or RGB-only data shown with '+' and 'x' symbols, respectively. Vertical bar indicates beginning of dredging (Nov 2013).

be affected greatly by the specific values used for these thresholds. As such, we do not advocate that these specific thresholds are applicable to other regions. Instead, these analyses indicate that thorough investigation of dredging-related turbidity should (at the minimum) include coarse assessment of these environmental parameters.

4.2. Measurement uncertainties

Ideally, an autonomous plume detection method using fixed thresholds for various products would need to be used to assess dredging impacts. However, in preliminary analyses, such approaches proved unreliable in this region. In several instances (e.g., Fig. 4 anomaly image on Julian day 11), the entirety of shallow water in this scene showed high anomalies for $R_{rs}(667)$ for reasons not completely understood. As such, using an "or" Boolean operator for autonomous delineation (high anomaly "or" high normalized anomaly) would be too inclusive. On the other hand, an "and" Boolean operator would be too narrow, as several plumes visible in RGB images show no associated elevation in $R_{rs}(667)$ anomaly or normalized anomaly (e.g., Fig. 4, Julian day 23). Furthermore, autonomous delineation using such anomaly thresholds is impossible when $R_{rs}(667)$ data are not available (due to thin clouds, high sensor zenith, sun glint, straylight contamination, etc.).

Although manual outlining is imprecise, it allows for more flexible integration of multiple data sources towards a final delineation and for refined plume delineation using a threshold. As with any such observer-based image analysis, the specific values used to scale the images (true color RGBs, PNGs of anomaly data, etc.) can inform the delineations. Furthermore, in order to allow for temporal clues in plume detection, the manual outlining was made in chronological order, which could introduce potential observer bias. To address this potential problem, several tests were repeated without knowledge of the time period (pre- or post- dredging), with the plume outlining results not differing from the original by more than 20%.

The specific wavebands used (667 nm for MODIS, 655 nm for Landsat) might also impact the results presented here. Specifically,

turbidity signals are muted in longer wavelengths, meaning higher SPM loads (or more strongly reflective particles) are necessary for detection of plumes using 865 nm data relative to 655 nm data. Indeed, much of the turbidity signal captured in this analysis using Landsat $\rho_w(655)$ data were not as easily apparent in $\rho_w(865)$ data. However, we found it more difficult to distinguish between water column turbidity and benthic contributions to the reflectance signal when considering Landsat $\rho_w(865)$ data. For MODIS data, the anomaly detection approach used was much more resilient to wavelength-dependent turbidity detection characteristics. Indeed, very similar results were seen for all 1 km resolution red wavebands (667, 678, 748, or 869 nm), while speckling prevented anomaly detection for $R_{rs}(645)$ and $R_{rs}(859)$ data.

Uncertainties also are introduced by the image processing (especially for MODIS), which can greatly impact the calculated areal extent of plumes. First, the large pixel size (250 × 250 m) of the RGB images is problematic, as turbidity features at a much finer-scale are obvious at higher resolution (Figs. 1 & 2). This problem is exacerbated by the extrapolation performed for $R_{rs}(667)$ data, which has native spatial resolution of 1 km at best. However, the before-after changes observed here, especially after ruling out cases due to environmental factors other than dredging, do not appear to be affected by the coarse resolution.

Nevertheless, due to these measurement uncertainties, the threshold delineated plumes are especially informative. Although this approach resulted in underestimations in certain cases (e.g. when a plume is clearly visible under thin clouds; Fig. 4 Julian Day 18), it constrains plume size based on objectively defined criteria. The success rate [number of delineated pixels with $R_{rs}(667)$ above the threshold divided by total number of pixels with valid $R_{rs}(667)$ data; 67% for this study] also provides a means by which the areal extent estimates of RGB-only outlines can be constrained.

Even without this constraint, however, the areal extents of RGB-only outlines were generally smaller than those made with the help of red band reflectance data [$R_{rs}(667)$ for MODIS, $\rho_w(655)$ for Landsat]. Indeed, two-tailed Wilcoxon rank sum tests indicated that the areal extents of RGB-only outlines were significantly different (smaller) than

Table 2
Size and frequency of occurrence for coral pixels included in turbidity plumes.

Delineation type	Time span	Number of images	Coral area impacted (km ²)	Average impact frequency (%)	Maximum impact frequency (%)
Manual outline	Pre-dredging	44	7.2	14	23
Manual outline	Post-dredging	142	12.9	23	70
Manual outline	Winter 2014	33	11.2	32	88
Manual outline	Spring 2014	31	8.4	37	81
Manual outline	Summer 2014	20	7.7	28	60
Manual outline	Autumn 2014	20	12.3	25	70
Threshold delineated	Pre-dredging	29	4.5	10	17
Threshold delineated	Post-dredging	91	11.2	16	38
Threshold delineated	Winter 2014	23	10.1	24	57
Threshold delineated	Spring 2014	16	7.2	24	44
Threshold delineated	Summer 2014	11	6.1	22	45
Threshold delineated	Autumn 2014	14	7.0	20	29

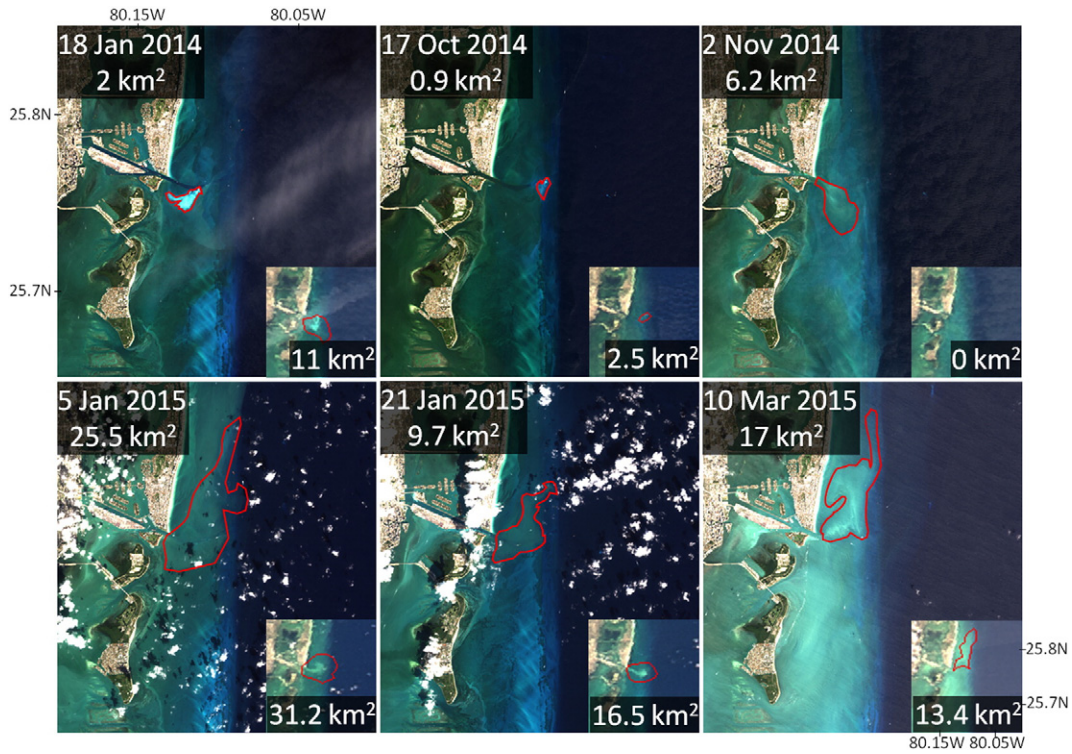


Fig. 11. Same-day Landsat and MODIS (insets) true color imagery. For these image pairs, the Landsat image precedes the MODIS image by approximately 2.5 h (overpass at 15:50 UTC for Landsat, 18:25 UTC for MODIS). Plume areal extent (km^2) indicated for each image.

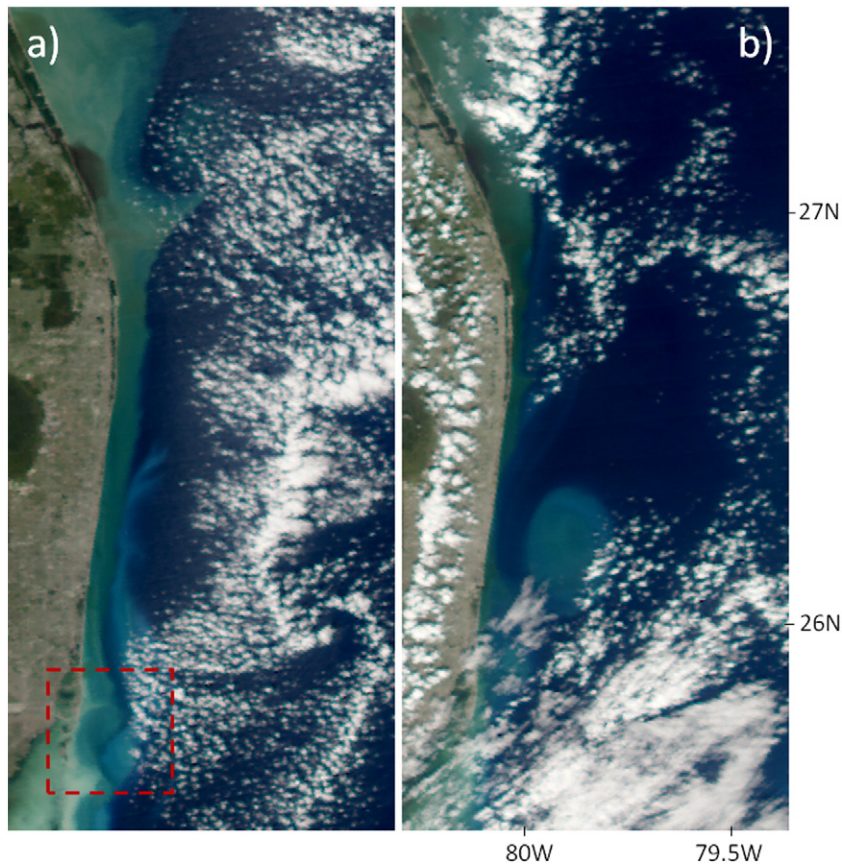


Fig. 12. MODIS true color imagery for the southeast Florida region from (a) 26 October 2005 (b) 27 October 2005, showing effects of a recent hurricane (a,b) and eddies (b) on regional water turbidity. The red box outlines the Port of Miami region as displayed in other figures.

those from days where reflectance data were available for both Landsat (Z-statistic = 2.6, $p < 0.01$) and MODIS (Z-statistic = 2.7, $p < 0.01$). For MODIS, this could result from the differences in native pixel sizes [> 250 m for RGB, > 1 km for $R_{rs}(667)$], as the same anomaly would be “larger” at a coarser spatial resolution. However, given that the same effect was observed for Landsat delineations (where only one spatial resolution was used), it is more likely that the added perspective offered by the reflectance data allowed for capture of plume effects outside that visible in RGB images.

Finally, settlement of the suspended sediment is a likely avenue for plume dispersal and a viable explanation for day-to-day plume variability. Such settlement, however, might change the benthic albedo, especially for coral covered regions (see Hochberg, Atkinson, & Andréfouët, 2003). Since the anomaly data were referenced against 2002–2012 climatologies, benthic albedo changes would potentially result in permanent anomalies, undermining a central assumption of this work. In practice, the relative sparseness of coral benthic cover combined with the large MODIS pixel size means any change in benthic albedo due to sediment settlement would be insignificant. Furthermore, permanent anomalies were not observed after dredging began (smaller plume size and frequency were observed during summer and autumn 2014 relative to winter and spring 2014, Figs. 9 and 10). As such, albedo shifts resulting from sediment settlement likely do not impact the results presented here.

4.3. Landsat or MODIS?

Both Landsat and MODIS are effective in revealing sediment plumes; the question then becomes which one to use to assess post-dredging plumes as they differ by spatial resolution and revisit frequency. The higher spatial resolution of Landsat data alleviates many of the uncertainties in MODIS-derived plumes. However, the low frequency of Landsat measurements is insufficient to capture the large temporal variability in plume size, shape, and extent, not to mention how to differentiate dredge-induced turbidity events from turbidity events induced by other factors. The lack of historical climatology in Landsat-derived reflectance also posed a problem in establishing a baseline to evaluate anomaly conditions. Ideally, high-quality and same-day measurements from MODIS and Landsat might be used to develop a scaling method to calibrate the more frequent MODIS observations to the more accurate Landsat observations. Unfortunately, only six same-day MODIS and Landsat image pairs were available for this entire time series (Fig. 11). The changes in plume shapes and sizes within the same day (Fig. 11) led to the conclusion that some of the differences between the same-day MODIS and Landsat observations (2.5 h apart) may be real. Thus, for this particular region it is nearly impossible to derive such scaling factors. Nevertheless, the temporal plume patterns observed from Landsat and MODIS generally agree with each other (Fig. 10), suggesting they may complement each other in assessing turbidity changes. For other regions, when Landsat-like sensors are available to provide more frequent measurements at the same 30-m resolution (e.g., a combination of HJ-1A and HJ-1B can provide a 2-day revisit of Chinese coastal waters), a constellation of 30-m resolution sensors (Landsat-7, Landsat-8, HJ-1A, HJ-1B) may provide high-resolution, high-frequency data to result in improved capacity for assessing turbidity and other water quality events. In addition, ESA's Sentinel-2A (and Sentinel-2B; planned launch in 2016) provides red and NIR reflectance at 10-m spatial resolution with 10 day (5 day combined) repeat sampling, thereby allowing even finer scale assessment of coastal water quality.

5. Conclusions

Despite the subjectivity in manual plume outlining and subsequent uncertainties in the determination of plume size, extent, and frequency, this study identifies regular, widespread turbidity plumes associated with dredging activity in the Port of Miami region. The conclusion is

based not only on time-series analysis of both Landsat and MODIS observations, but also on the established rules to discount the natural turbidity events due to other environmental factors. The ephemeral nature of these plumes, combined with in situ reports of large scale sedimentation of coral communities, strongly indicates potentially widespread ecological damage. Overall, the methods described here provide a framework by which turbidity plumes resulting from human activities can be assessed and monitored in coastal, optically complex regions. As dredging activities are scheduled for other areas (including those with nearby coral communities such as Port Everglades, FL), similar work should be completed as part of the real-time monitoring of dredging activities in order to more appropriately assess turbidity plumes and potentially mitigate environmental damage.

Acknowledgments

The authors wish to thank the many organizations that provided data used in this analysis, including NASA GSFC, USGS, Florida Fish and Wildlife Conservation Commission (FWC) FWRI, NOAA NCDC, NOAA NGDC, NOAA NDBC, and NOAA tides and currents. The authors also wish to thank Captain Dan Kipnis for providing the aerial photographs in Fig. 1, and two anonymous reviewers whose contributions greatly improved this manuscript. Funding for this research was provided by NASA's OBB program and water quality program, as well as NOAA's Coral Watch program through the Cooperative Institute for Marine and Atmospheric Studies.

References

- Baith, K., Lindsay, R., Fu, G., & McClain, C.R. (2001). Data analysis system developed for ocean color satellite sensors. *Eos, Transactions American Geophysical Union*, 82(18), 202–202. <http://dx.doi.org/10.1029/01E000109>.
- Barnes, B.B., & Hu, C. (2015). Cross-sensor continuity of satellite-derived water clarity in the gulf of Mexico: Insights into temporal aliasing and implications for long-term water clarity assessment. *IEEE Transactions on Geoscience and Remote Sensing*, 53(4), 1761–1772.
- Barnes, B.B., Hu, C., Holekamp, K.L., Blonski, S., Spiering, B.A., Palandro, D.A., & Lapointe, B. (2014). Use of Landsat data to track historical water quality changes in Florida Keys marine environments. *Remote Sensing of Environment*, 140, 485–496. <http://dx.doi.org/10.1016/j.rse.2013.09.020>.
- Barnes, B.B., Hu, C., Schaeffer, B.A., Lee, Z., Palandro, D.A., & Lehrter, J.C. (2013). MODIS-derived spatiotemporal water clarity patterns in optically shallow Florida Keys waters: A new approach to remove bottom contamination. *Remote Sensing of Environment*, 134, 377–391. <http://dx.doi.org/10.1016/j.rse.2013.03.016>.
- Bokuniewicz, H.J., & Gordon, R.B. (1980). Deposition of dredged sediment at open water sites. *Estuarine and Coastal Marine Science*, 10, 289–303.
- Chassignet, E.P., Hurlburt, H.E., Smedstad, O.M., Halliwell, G.R., Hogan, P.J., Wallcraft, A.J., ... Bleck, R. (2007). The HYCOM (HYbrid Coordinate Ocean Model) data assimilative system. *Journal of Marine Systems*, 65(1–4 SPEC. ISS.), 60–83. <http://dx.doi.org/10.1016/j.jmarsys.2005.09.016>.
- Dial Cordy and Associates Inc (2015). *Delineation of potential sedimentation effect area within middle and outer reef habitats*. Port of Miami phase III federal channel expansion project FDEP Permit #0305721-001-BI.
- Dogliotti, A.I., Ruddick, K.G., Nechad, B., Doxaran, D., & Knaeps, E. (2015). A single algorithm to retrieve turbidity from remotely-sensed data in all coastal and estuarine waters. *Remote Sensing of Environment*, 156, 157–168. <http://dx.doi.org/10.1016/j.rse.2014.09.020>.
- Doxaran, D., Cherukuru, N., & Lavender, S.J. (2006). Apparent and inherent optical properties of turbid estuarine waters: Measurements, empirical quantification relationships, and modeling. *Applied Optics*, 45(10), 2310–2324. <http://dx.doi.org/10.1364/AO.45.002310>.
- Erfemeijer, P.L. a., Riegl, B., Hoeksema, B.W., & Todd, P. a. (2012). Environmental impacts of dredging and other sediment disturbances on corals: A review. *Marine Pollution Bulletin*, 64(9), 1737–1765. <http://dx.doi.org/10.1016/j.marpolbul.2012.05.008>.
- FDEP (2012). *Consolidated environmental resource permit and sovereign submerged lands authorization*. Tallahassee, FL: Florida department of environmental protection (46 pp.).
- FDEP (2014). *Warning letter of possible violations and non-compliance, miami harbor phase III federal channel expansion, permit no. 0305721-001-BI*. Tallahassee, FL: Florida Department of Environmental Protection (5 pp.).
- Feng, L., Hu, C., Chen, X., Tian, L., & Chen, L. (2012). Human induced turbidity changes in Poyang Lake between 2000 and 2010: Observations from MODIS. *Journal of Geophysical Research, Oceans*, 117(7) <http://dx.doi.org/10.1029/2011JC007864>.
- Goreau, T., McClanahan, T., Hayes, R., & Strong, A. (2000). Conservation of coral reefs after the 1998 global bleaching event. *Conservation Biology*, 14(1), 5–15.
- Hadjimitsis, D.G., Hadjimitsis, M.G., Clayton, C., & Clarke, B. a. (2006). Determination of turbidity in Kourris Dam in Cyprus utilizing Landsat TM remotely sensed data.

- Water Resources Management*, 20(3), 449–465. <http://dx.doi.org/10.1007/s11269-006-3089-y>.
- He, M.-X., Hu, L., & Hu, C. (2014, July). Harbour dredging and fish mortality in an aquaculture zone: assessment of changes in suspended particulate matter using multi-sensor remote-sensing data. *International Journal of Remote Sensing*, 37–41. <http://dx.doi.org/10.1080/01431161.2014.916446>.
- Hochberg, E.J., Atkinson, M.J., & Andréfouët, S. (2003). Spectral reflectance of coral reef bottom-types worldwide and implications for coral reef remote sensing. *Remote Sensing of Environment*, 85(2), 159–173. [http://dx.doi.org/10.1016/S0034-4257\(02\)00201-8](http://dx.doi.org/10.1016/S0034-4257(02)00201-8).
- Hu, C. (2011). An empirical approach to derive MODIS ocean color patterns under severe sun glint. *Geophysical Research Letters*, 38(1) <http://dx.doi.org/10.1029/2010GL045422>.
- Hu, C., Chen, Z., Clayton, T.D., Swarzenski, P., Brock, J.C., & Muller-Karger, F.E. (2004). Assessment of estuarine water-quality indicators using MODIS medium-resolution bands: Initial results from Tampa Bay, FL. *Remote Sensing of Environment*, 93(3), 423–441. <http://dx.doi.org/10.1016/j.rse.2004.08.007>.
- Hu, C., Muller-Karger, F.E., Andréfouët, S., & Carder, K.L. (2001). Atmospheric correction and cross-calibration of LANDSAT-7/ ETM + imagery over aquatic environments: A multiplatform approach using SeaWiFS/ MODIS. *Remote Sensing of Environment*, 78, 99–107.
- Islam, M.R., Yamaguchi, Y., & Ogawa, K. (2001). Suspended sediment in the Ganges and Brahmaputra Rivers in Bangladesh: Observation from TM and AVHRR data. *Hydrological Processes*, 15(3), 493–509. <http://dx.doi.org/10.1002/hyp.165>.
- Kourafalou, V.H., & Kang, H. (2012). Florida current meandering and evolution of cyclonic eddies along the Florida keys reef tract: Are they interconnected? *Journal of Geophysical Research, Oceans*, 117(5), 1–25. <http://dx.doi.org/10.1029/2011JC007383>.
- Lathrop, R.G., Lillesand, T.M., & Yandell, B.S. (1991). Testing the utility of simple multi-date Thematic Mapper calibration algorithms for monitoring turbid inland waters. *International Journal of Remote Sensing*, 12(10), 2045–2063. <http://dx.doi.org/10.1080/01431169108955235>.
- Lee, T.N. (1975). Florida current spin-off eddies. *Deep Sea Research and Oceanographic Abstracts*, 22(11), 753–765. [http://dx.doi.org/10.1016/0011-7471\(75\)90080-7](http://dx.doi.org/10.1016/0011-7471(75)90080-7).
- Matthews, M.W. (2011). A current review of empirical procedures of remote sensing in inland and near-coastal transitional waters. *International Journal of Remote Sensing*, 32(21), 6855–6899. <http://dx.doi.org/10.1080/01431161.2010.512947>.
- Mertes, L., Smith, M., & Adams, J. (1993). Estimating suspended sediment concentrations in surface waters of the Amazon River wetlands from Landsat images. *Remote Sensing of Environment*, 43(3), 281–301. [http://dx.doi.org/10.1016/0034-4257\(93\)90071-5](http://dx.doi.org/10.1016/0034-4257(93)90071-5).
- Miller, R.L., & McKee, B.A. (2004). Using MODIS Terra 250 m imagery to map concentrations of total suspended matter in coastal waters. *Remote Sensing of Environment*, 93(1–2), 259–266. <http://dx.doi.org/10.1016/j.rse.2004.07.012>.
- Mulligan, R.F., & Lombardo, G.A. (2011). Panama Canal expansion: Alleviating global climate change. *WMU Journal of Maritime Affairs*, 10(1), 97–116. <http://dx.doi.org/10.1007/s13437-011-0008-8>.
- NOAA NMFS(2015). Port of Miami *Acropora cervicornis* Relocation Report: NOAA National Marine Fisheries Service.
- Ouillon, S., Douillet, P., & Andréfouët, S. (2004). Coupling satellite data with in situ measurements and numerical modeling to study fine suspended-sediment transport: A study for the lagoon of New Caledonia. *Coral Reefs*, 23(1), 109–122. <http://dx.doi.org/10.1007/s00338-003-0352-z>.
- Palandro, D. a., Andréfouët, S., Hu, C., Hallock, P., Müller-Karger, F.E., Dustan, P., ... Beaver, C.R. (2008). Quantification of two decades of shallow-water coral reef habitat decline in the Florida Keys National Marine Sanctuary using Landsat data (1984–2002). *Remote Sensing of Environment*, 112(8), 3388–3399. <http://dx.doi.org/10.1016/j.rse.2008.02.015>.
- Patt, F.S., Barnes, R.A., Eplee, R.E., Franz, B.A., Robinson, W.D., Feldman, G.C., ... Yoder, J.A. (2003). Algorithm updates for the Fourth SeaWiFS Data Reprocessing. In S.B. Hooker, & E.R. Firestone (Eds.), *NASA Tech Memo 2003–206892. SeaWiFS Postlaunch Technical Report Series Vol. 22*.
- Petus, C., Chust, G., Gohin, F., Doxaran, D., Froidefond, J.M., & Sagarminaga, Y. (2010). Estimating turbidity and total suspended matter in the Adour River plume (South Bay of Biscay) using MODIS 250-m imagery. *Continental Shelf Research*, 30(5), 379–392. <http://dx.doi.org/10.1016/j.csr.2009.12.007>.
- Philipp, E., & Fabricius, K. (2003). Photophysiological stress in scleractinian corals in response to short-term sedimentation. *Journal of Experimental Marine Biology and Ecology*, 287(1), 57–78. [http://dx.doi.org/10.1016/S0022-0981\(02\)00495-1](http://dx.doi.org/10.1016/S0022-0981(02)00495-1).
- Pollock, F.J., Lamb, J.B., Field, S.N., Heron, S.F., Schaffelke, B., Shedrawi, G., ... Willis, B.L. (2014). Sediment and turbidity associated with offshore dredging increase coral disease prevalence on nearby reefs. *PLoS ONE*, 9(7) <http://dx.doi.org/10.1371/journal.pone.0102498>.
- Ritchie, J.C., & Cooper, C.M. (1988). Comparison of measured suspended sediment concentrations with suspended sediment concentrations estimated from Landsat MSS data. *International Journal of Remote Sensing*, 9(3), 379–387. <http://dx.doi.org/10.1080/01431168808954861>.
- Rogers, C. (1990). Responses of coral reefs and reef organisms to sedimentation. *Marine Ecology Progress Series*, 62, 185–202. <http://dx.doi.org/10.3354/meps062185>.
- Sampson, H. (2015, February 26). 2014 tourist tally: 14.5 million in Miami-Dade. The Miami Herald. (Retrieved from <http://www.miamiherald.com/>)
- Shi, W., Wang, M., & Jiang, L. (2011). Spring-neap tidal effects on satellite ocean color observations in the Bohai Sea, Yellow Sea, and East China Sea. *Journal of Geophysical Research, Oceans*, 116(12), 1–13. <http://dx.doi.org/10.1029/2011JC007234>.
- Shi, W., Wang, M., & Jiang, L. (2013). Tidal effects on ecosystem variability in the Chesapeake Bay from MODIS-Aqua. *Remote Sensing of Environment*, 138, 65–76. <http://dx.doi.org/10.1016/j.rse.2013.07.002>.
- US Department of Commerce (2014). Endangered and threatened wildlife and plants: Final listing determinations on proposal to list 66 reef-building coral species and to reclassify elkhorn and staghorn corals. *Federal Register*, Vol. 79, (No. 175, Docket No. 0911231415–4826–04; RIN 0648–XT12).
- Vanhellemont, Q., & Ruddick, K. (2014). Turbid wakes associated with offshore wind turbines observed with Landsat 8. *Remote Sensing of Environment*, 145, 105–115. <http://dx.doi.org/10.1016/j.rse.2014.01.009>.
- Vanhellemont, Q., & Ruddick, K. (2015). Advantages of high quality SWIR bands for ocean colour processing: Examples from Landsat-8. *Remote Sensing of Environment*, 161, 89–106. <http://dx.doi.org/10.1016/j.rse.2015.02.007>.
- Wang, J. -J., Lu, X.X., Liew, S.C., & Zhou, Y. (2009). Retrieval of suspended sediment concentrations in large turbid rivers using Landsat ETM +: An example from the Yangtze River, China. *Earth Surface Processes and Landforms*, 34(8), 1082–1092. <http://dx.doi.org/10.1002/esp.1795>.